J. Fluid Mech. (1999), *vol.* 389, *pp.* 81–99. Printed in the United Kingdom

Quasi-periodic state and transition to turbulence in a rotating Couette system

By YASUSHI TAKEDA

Paul Scherrer Institut, CH 5232 Villigen, Switzerland

(Received 1 March 1996 and in revised form 17 August 1998)

An experimental study of flow transition in a rotating Taylor–Couette system was made by investigating the spatio–temporal velocity field (axial velocity component) by the ultrasonic Doppler method. The flow fields for the range of Reynolds numbers $9 < R^* < 40$ (where $R^* = R/R_c$; R_c is the critical Reynolds number for Taylor vortex flow) were decomposed by two-dimensional Fourier transform and the orthogonal decomposition technique, and intensities of coherent structural modes were quantitatively obtained. The variation of the intensities of various modes with respect to Reynolds number clearly shows a transition behaviour of the quasi-periodic state resulting from the wavy vortex mode and the modulating waves, which is found to disappear suddenly at about $R^* = 21$. A new mode was found after the disappearance of the quasi-periodic state, which in turn disappears at $R^* = 36$. Beyond this regime, there was no coherent structure found except for the stationary Taylor vortices and so-called broad-band component, which is attributed to chaos. The total energy occupation (the number of modes which occupy 90% of the total energy) and the global entropy support such transition behaviour quantitatively. After the disappearance of the newly found mode, the number of modes needed to compose the velocity field is still finite and small – about 40–50. We call this flow state 'soft turbulence'.

1. Introduction

Following the investigation by Coles (1965), the flow between rotating cylinders (Taylor–Couette system) has often been used to investigate the transition from laminar to turbulent fluid motion (see Di Prima & Swinney 1985). The following sequence of flow regimes has been observed in narrow-gap systems with a rotating inner cylinder and a stationary outer cylinder.

At very low Reynolds numbers (R) one finds two-dimensional circular Couette flow (CF) which (for infinitely long cylinders) has the velocity profile $\boldsymbol{V} = (0, V_\theta(r), 0)$. At $R = R_c$ Couette flow becomes unstable to Taylor-vortex flow (TVF), a three-dimensional, time-independent flow structured into a set of stacked axisymmetric counter-rotating toroidal vortices. On increasing R past a second critical Reynolds number R_w, an instability sets in which deforms a Taylor vortex to produce a time-dependent non-axisymmetric flow called wavy vortex flow (WVF). On increasing R further an additional wave mode appears which modulates WVF; this flow is called modulated wavy vortex flow (MWV). Coughlin *et al.* (1991) reported that there are two different modes for MWV and that for some parameter ranges they coexist. The GS mode (Gorman & Swinney 1979) characteristically extends over the roll and is a wave component for a modulation, leading to a periodic flattening of the outflow boundary of the vortices. The ZS mode (Zhang & Swinney 1985) appears near the

outflow region with a higher phase speed inducing the appearance of a ripple on the roll. Experimental confirmation of their coexistence was reported by Takeda, Fischer & Sakakibara (1993*a*).

At the next transition ($R^* = R/R_c \approx 12$) a broad peak appears in the velocity power spectra and there is a rise in the background noise level (Fenstermacher, Swinney & Gollub 1979). This transition has been carefully studied using nonlinear time series techniques by Brandstater & Swinney (1987) who conclude that the flow dynamics fit the description of deterministic chaos, even though the transition itself seems not to be understood mathematically. Consequently it seems safe to classify the resulting flow as chaotic wavy vortex flow (CWV).

On further increasing the Reynolds number many investigators have observed that the azimuthal waves disappear at some critical Reynolds number and that the flow is then turbulent, even though the Taylor vortex structure remains (Coles 1965; Burkhalter & Koschmieder 1973; Fenstermacher *et al.* 1979; Walden & Donnelly 1979). The resulting flow is called turbulent Taylor vortex flow (TTV). Qualitatively it might be described as having a small 'turbulently' varying flow field superimposed on an axisymmetric mean field.

Thus far the transition from CWV to TTV has not been studied with the same degree of care as the transition to CWV. The objective of the present investigation is to clarify (i) how CWV behaves at higher R until its disappearance, and (ii) what occurs on the transition to TTV. Since this transition involves a strong change of a spatio–temporal nature, it is important to investigate the flow field in the spatio-temporal domain. We used an ultrasound Doppler technique to obtain spatio–temporal velocity fields and analysed them by two-dimensional Fourier analysis and orthogonal decomposition (principal component analysis). Both methods yield spectra which give information on the energy of the flow field. We then discuss the transition sequence from laminar flow to turbulence based on a quantitative evaluation of these two kinds of spectra, and suggest that TTV be interpreted as 'soft' turbulence (see Heslot, Castaing & Libchaber 1987).

2. Experimental setup

We used the same experimental setup as in our previous investigation (Takeda *et al.* 1993*b*). Briefly, our Taylor–Couette system (figure 1) has a radius ratio $\eta = R_i/R_o = 0.904$ (R_i is the radius of the inner cylinder, 94.0 mm, and R_o that of the outer cylinder, 104.0 mm) and aspect ratio $\Gamma = L/d = 20$ ($d = R_o - R_i, L$ is the fluid height). Only the inner cylinder is rotated. The Reynolds number R is defined as $R = \Omega R_i d/\nu$ (Ω is the frequency of rotation of the inner cylinder, ν is the kinematic viscosity), and the reduced Reynolds number is defined $R^* = R/R_c$. In the present configuration, the critical Reynolds number R_c for the onset of TVF is 134.57 (see Di Prima & Swinney 1985). The liquid used in these experiments was a mixture of water and 30% glycerol.

The measurements were carried out with an ultrasonic velocity profile monitor, which can obtain a time series of instantaneous velocity profiles (Takeda 1986, 1990; Teufel *et al.* 1992). The ultrasonic transducer was affixed to the outer surface of one of the stationary endwalls, being perpendicular to it with its centre on the outer cylinder wall position. The diameter of the ultrasonic beam was 5 mm. This setup measures the velocity profile of the axial velocity component as a function of axial position and time, namely $V_z(z,t)$ at the outer wall position. Thus the measuring volume of one point is one half of a disk with a radius 2.5 mm and a thickness 0.75 mm. The

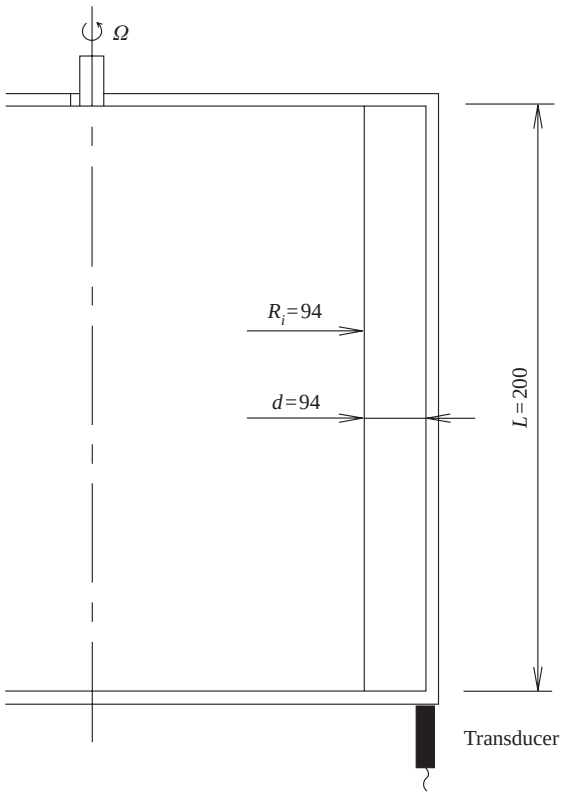

FIGURE 1. Schematic of the experimental system.

present system measures velocities at 128 spatial positions. The measurement of the velocity profile was focused on the spatial range from 40 mm to 135 mm (i.e. from $z = 4d$ to $13.5d$) from the endwall in order to eliminate any endwall effect. This setup of the UVP required a measuring time of 130 ms for each profile for a velocity level of a few mm s^{-1}. A total of 1024 successive profiles were recorded in the instrument's memory and then transferred to disk for later analysis.

We performed the measurements for R^* ranging from approximately 10 to > 40 for most runs. This covers the flow regimes MWV, for which onset is at $R^* \approx 9$, CWV, TTV etc. For most of the measurements we started from the highest R^* and decreased it in small steps. This protocol was used because we felt that no new unstable flow mode would be excited by changing the Reynolds number in this way, and that the waiting time between measurements could be minimized.

3. Experimental results

3.1. *Display of velocity profiles*

Since we obtain the axial component of the velocity field as a function of position and time, the results are displayed in colour density plots like those in figure 2. When presented in this form, the abscissa is time and the ordinate is axial position. The velocity values are colour-coded: red-violet for positive values (motion directed away from the transducer) and blue-green for negative. A horizontal band (wavy or not) of the same flow direction (reddish or blueish) corresponds to a single Taylor

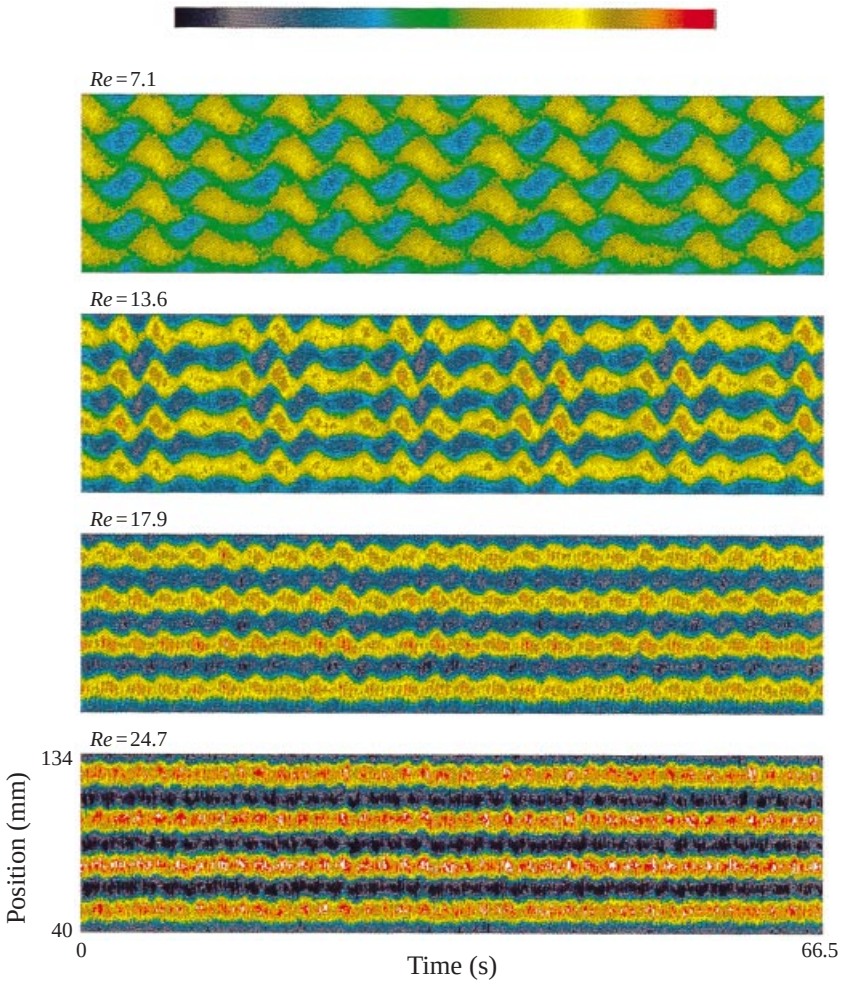

FIGURE 2. Examples of measured velocity fields for four Reynolds numbers. Displayed are 256 profiles over a 66.5 s time period and 128 positional positions for 74 mm. Velocity values are colour coded as given at the top. Red-yellow is for positive and blue-green for negative velocity.

vortex. Figure 2 shows a clear change of flow structure: WVF at $R^* = 7.1$, CWV at $R^* = 13.6$ and 17.9, and TTV at $R^* = 24.7$. The wavy structure at $R^* = 7.1$ indicates that the roll moves up and down due to a propagating azimuthal wave. At $R^* = 13.6$ modulation due to the GS mode can be clearly seen, with a diminished amplitude at $R^* = 17.9$. For $R^* > 21$, coherent oscillatory motion disappears and again the boundaries between vortices become flat (on average), although small-scale motion remains inside each roll and its boundaries.

3.2. *Time and space domain Fourier analysis*

We performed a one-dimensional Fourier analysis of the data set: power spectrum and energy spectral density. These spectra were computed by fast Fourier transformation (FFT) in the time and space domains independently, yielding space-dependent power spectra and time-dependent energy spectra for all the data concerned. Although certain characteristics were observed to be space-dependent in the power spectra and

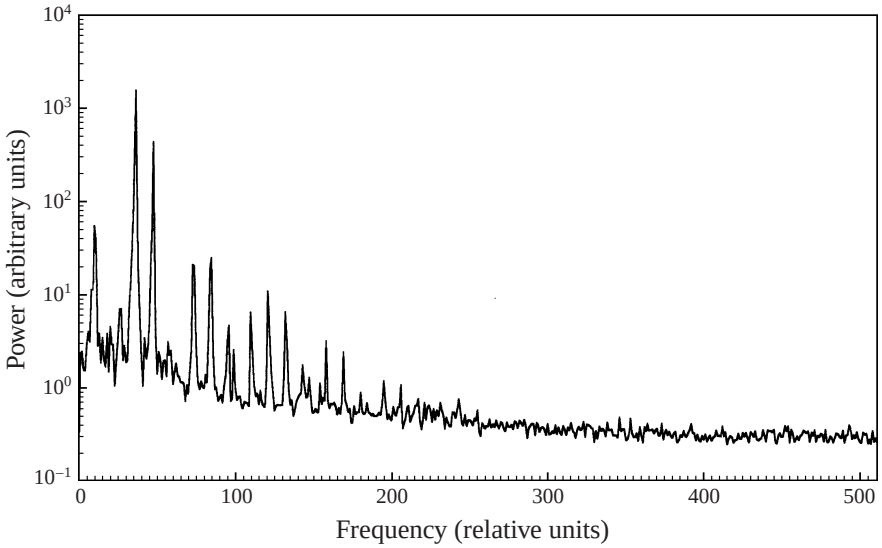

FIGURE 3. A space-averaged power spectrum (R^*=13.6). The original velocity field is in figure 2.

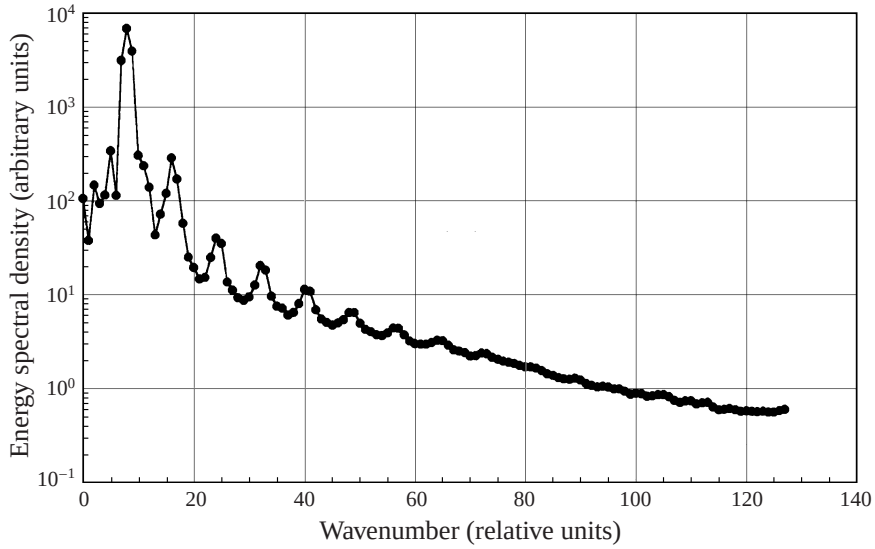

FIGURE 4. A time-averaged energy spectral density for the same data as in figure 3.

time-dependent in the energy spectra, we focused our attention on space averages of the power spectrum (figure 3) and time averages of the energy spectrum (figure 4). Clear peak structures were seen in both kinds of spectra although the structure was more complex in the power spectrum as figure 3 shows. We found the energy spectrum to be less informative in this study, since all the peaks fall on higher harmonics of the fundamental mode, which corresponds to the axial wavelength of the Taylor vortex.

An analysis of the power spectra was carried out by identifying each peak in a spectrum as either a fundamental, a harmonic of a fundamental, or a linear combination of two or more fundamental frequencies. We found that there are three

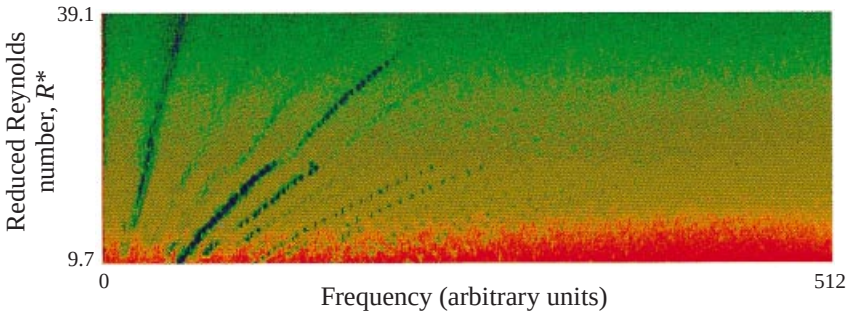

FIGURE 5. Variation of the space-averaged power spectra on the (R^*, f)-plane. The power value is colour coded as in figure 2 but on a relative scale.

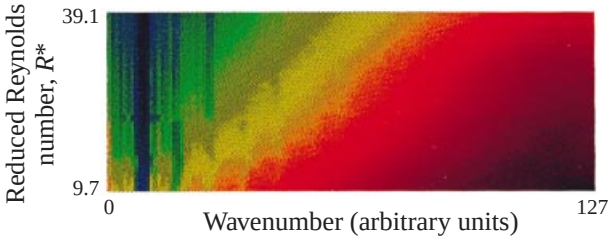

FIGURE 6. Variation of the time-averaged energy spectral density on the (R^*, k)-plane. Colour coding is the same as for figure 5.

intrinsic wave modes for the MWV regime: the WVF, GS and ZS modes. Furthermore we found that all three modes can coexist. We also found that a significant change in the flow characteristics occurs at $R^* = 21$, where the azimuthal wave mode (WVF mode) disappears. That is, the magnitude of power and energy of higher harmonic modes behaves very differently for $R^* > 21$ than for $R^* < 21$. We have reported this finding in Takeda *et al.* (1993*a*). Figure 5 is a two-dimensional colour plot of the space-averaged power spectra, as a function of frequency and Reynolds number. Because our measurement consisted of irregular increments of the Reynolds number, the iso-power lines are not smooth in this plot. A quasi-continuous curve nevertheless corresponds to a single temporal mode. In a plot such as this, the appearance and disappearance of various temporal modes and their harmonics at various Reynolds number are better displayed. Thus a drastic change of behaviour which occurs at $R^* \approx 21$ is clearly seen in this figure. Many temporal modes disappear at this Reynolds number and only a few higher modes remain beyond this point. Figure 6 is constructed similarly to figure 5 but shows the energy spectral density as a function of Reynolds number. In this case, the iso-power lines are straight and vertical since the wavenumber of each mode does not change with Reynolds number. This figure thus shows the same behaviour of each mode versus R^* as in figure 5.

3.3. *Mode identification*

We mainly used one-dimensional Fourier analysis for mode identification. As seen in figure 5, peaks of the same mode form curved lines, since the peak frequency depends on the rotational speed (or equivalently the Reynolds number). Moreover, these lines appear and disappear, and they thus reflect the sequence of flow transition from WVF to turbulence. By using this plot, peaks in each power spectrum have been assigned and identified, and then intrinsic modes in the flow were detected. The intensity of

these peaks was evaluated by estimating their areas, and subsequently the variation with respect to R^* was obtained. From this analysis we found the coexistence of several modes and the disappearance of the WVF and MWV modes (Takeda *et al.* 1993*b*).

3.4. *Two-dimensional Fourier analysis*

For investigating the nature of the quasi-periodic state quantitatively, a time-domain Fourier analysis is not sufficient, since various spatial modes contribute to the same peak in the power spectrum. It is therefore necessary to decompose the velocity field with respect to space and time simultaneously, because the nature of this flow is solely spatio–temporal. We used a two-dimensional Fourier transformation in this study, since this flow configuration exhibits both spatial and temporal periodicity. A two-dimensional FFT was computed on space and time coordinates as

$$S(f,k) = \int_{\infty}^{\infty} \int_{\infty}^{\infty} V_z(z,t)\mathrm{e}^{-\mathrm{i}kx}\mathrm{e}^{-\mathrm{i}ft}\mathrm{d}x\mathrm{d}t, \tag{3.1}$$

where f is a frequency and k a wavenumber. For the present experimental setup, with respect to the space and time resolution, we can obtain a two-dimensional Fourier spectrum on the plane of $f = [0, 7.57]$ (Hz) and $k = [0, 1.33]$ (mm^{-1}) with resolutions of [14.8 mHz, 0.010 mm^{-1}].

An example of the results is given by the surface plot in figure 7. The resulting Fourier spectrum has many isolated peaks reflecting the highly spatio–temporal nature of the flow field. Each peak corresponds to a wave mode or its higher harmonic in a two-dimensional sense. We adopted a 'numerical filtering' strategy to investigate the flow: a filtered velocity field is constructed by setting to zero the power in unwanted frequencies of the raw Fourier spectrum and then inverse Fourier transforming the result. Using such a decompositional analysis, we found that the so-called broad-band component, which is attributed to chaos, corresponds to a flow motion that moves from vortex to vortex (Takeda, Fischer & Sakakibara 1994).

3.5. *Orthogonal decomposition*

Beyond the flow regime of the quasi-periodic state, the flow structure becomes less periodic and Fourier analysis is less effective. For investigating such cases, an orthogonal decomposition is well suited since it allows maximal data compression by catching characteristic features of the eigenmode. Moreover, the eigenvalue spectrum can be used to investigate the changing complexity of the flow with respect to Reynolds number. Thus, the same data sets have been analysed using an orthogonal decomposition technique. There exists in the literature a number of such techniques: proper orthogonal decomposition (Lumley 1967, 1981; Berkooz, Holmes & Lumley, 1993), bi-orthogonal decompositon (Aubry, Chauve & Guyonnet 1994), singular system analysis (Broomhead & King 1986), Karhunen–Loeve decomposition, empirical eigenfunction decomposition (Sirovich 1991) etc. As made clear by Drazin & King (1992), all these techniques involve a calculation and analysis of the eigenvalues and eigenvectors of a covariance matrix constructed from the data, and hence are equivalent.

From each measurement we obtain a time series of velocity profiles and store it in an $M \times N = 1024(\mathsf{time}) \times 128(\mathsf{space})$ matrix $\boldsymbol{V}$. Thus the jth row of $\boldsymbol{V}$ is the velocity profile at time j, and the kth column of $\boldsymbol{V}$ is the velocity time series at spatial position k. Most of the kinetic energy of the motion is contained in the Taylor-vortex motion. We are mainly interested in the fluctuation around this state. Therefore, we compute

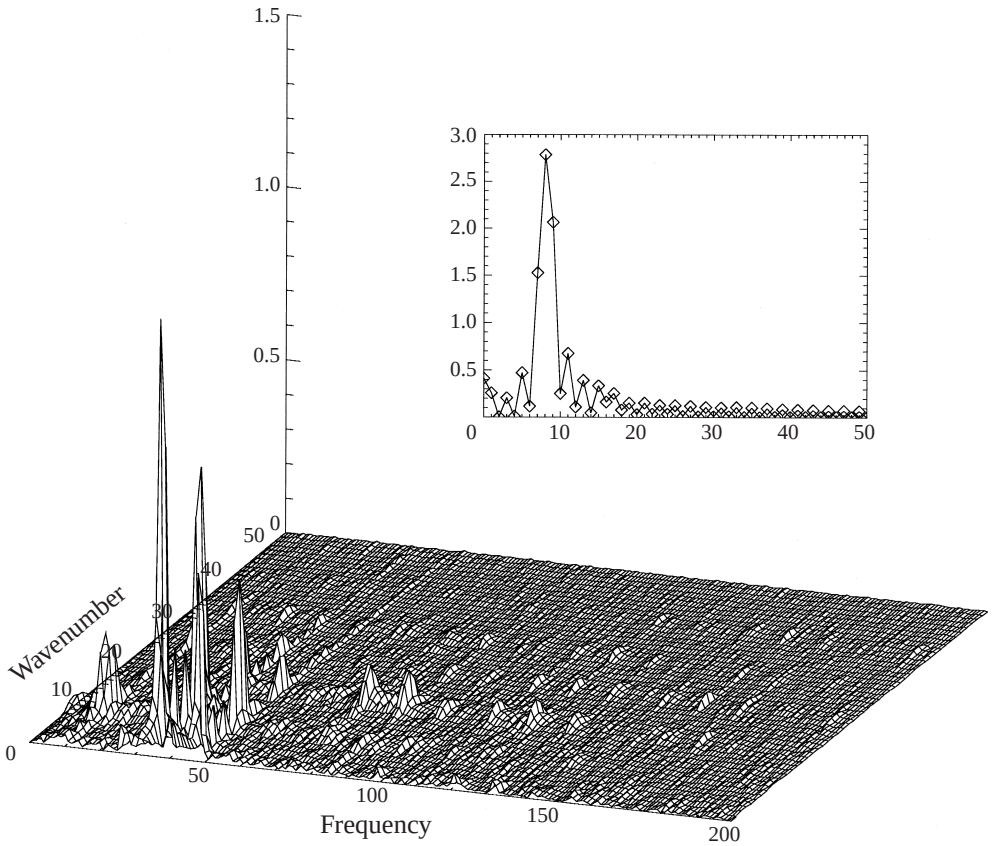

FIGURE 7. A portion of the surface plot of the two-dimensional Fourier spectrum for the same data as for figure 3. The insert is a k-spectrum at $f = 0$ for a clearer view.

and subtract the mean profile from the raw data matrix, compute the covariance matrix of the result, and process it with the appropriate eigenvalue decomposition algorithm. More specifically,

(i) Compute the mean profile $\bar{\boldsymbol{v}}$ from the raw data matrix:

$$\bar{v}_j = \frac{1}{M} \sum_{i=1}^{M} V_{ij},$$

where M is the length of the time series.

(ii) Subtract $\bar{\boldsymbol{v}}$ from each row of $\boldsymbol{V}$ and store the result in $\boldsymbol{U}$: $U_{ij} = V_{ij} - \bar{v}_j$ $(i = 1, \ldots, M, j = 1, \ldots, N)$.

(iii) Compute the $N \times N$ covariance matrix: $\boldsymbol{C} = \boldsymbol{U}^t \boldsymbol{U}/M$, where t denotes transpose.

(iv) Compute the eigenvalues $\{e_j\}_{j=1,\ldots,N}$ and eigenvectors $\{\boldsymbol{f}_j\}_{j=1,\ldots,N}$ of $\boldsymbol{C}$.

(v) Sort the eigenvalues in descending order, i.e. $e_1 \geqslant e_2 \geqslant \cdots \geqslant e_N$.

Note that the eigenvectors are elemental spatial patterns of the fluctuation velocity field. The eigenvalues yield information about the contribution of the corresponding elemental patterns to the velocity field, and hence contribute information about the number of important spatial degrees of freedom.

The computed eigenvalue spectrum and the eigenvectors corresponding to the

eight largest eigenvalues are shown for $R^* = 13.6$ in figure 8(a) and for $R^* = 24.7$ in figure 8(b). The vector labelled 'mode index 0' is the time-averaged velocity profile (and hence corresponds to the basic TVF mode), which was included intentionally for display purposes. In both cases, the eigenvalue spectrum shows a very sharp decrease for the initial modes and thereafter shows a slow decay. This implies that only a few modes are necessary to describe the velocity field. The shape of the eigenvectors shows a low-frequency character for the first five modes at $R^* = 13.6$ and for only three modes at $R^* = 24.7$. For mode indices 4, 5 and larger, the eigenvectors are high frequency and can most likely be considered as flow noise.

4. Discussion

4.1. *Two-dimensional Fourier analysis*

4.1.1. *WVF and MWV*

Since each mode is well decomposed and resolved in the two-dimensional Fourier spectrum as shown in figure 7, we obtained the magnitude of each individual mode (spatio–temporal component) by estimating the volume of each peak. We did this to quantitatively investigate the flow transition and the behaviour of these modes. For the prominent peaks in all our data sets, a peak volume was estimated for a 3 unit by 3 unit area of the Fourier spectrum. This corresponds to a resolution of 44.4 mHz for frequency and 0.03 mm^{-1} for wavenumber. Peaks on the $f = 0$ edge of the spectrum plane correspond to the time-averaged velocity profile (Taylor vortices) and will not be discussed here.

The variation of mode intensity, obtained as above, with respect to Reynolds number is plotted in figure 9. The higher harmonics of wavenumber as well as of frequency are observed to behave similarly to their basic modes. There are three distinct groups of lines observed in this plot, which correspond to three coherent modes of MWV. The first mode prevails at the lowest R^* studied here ($R^* < 10$). It already has a significant intensity at the lowest Reynolds number, and is fairly constant for $R^* < 21$. The second group appears at R^* slightly lower than 10 and increases logarithmically until $R^* = 17$, beyond which it stays constant. At $R^* \approx 21$, both of these modes disappear quite suddenly. They are still observed at $R^* = 21$–22, but the decrease is sharp, by two orders of magnitude. Beyond this R^*, after the disappearance of the above two modes, a new mode appears at $R^* = 23$. The intensity of this mode shows a smooth increase from its inception at $R^* = 23$, reaches a maximum at $R^* = 29$, and then shows a steady decrease until its disappearance at $R^* = 36$. The behaviour described above for these three distinctive curves is the same for all higher harmonic components within the group, although their intensities are smaller than the basic and lower harmonic modes. That is, although similar, the ascending sequence of harmonics is smaller in magnitude by a factor of roughly five.

The first mode described above is easily identified as the WVF mode, since it is the only mode appearing for $R^* < 10$. The second mode corresponds to one of two kinds of MWV modes, namely GS or ZS. The onset of this mode is at approximately $R^* = 11$, which is in agreement with Gorman & Swinney (1979). The subsequent sudden disappearance of these two modes can be considered to correspond to the disappearance of the azimuthal wave. In fact, such a disappearance has been observed often and reported earlier (for example, Koschmieder 1980; Walden & Donnelly 1979), as an evidence of a transition to turbulence, in general, in this configuration.

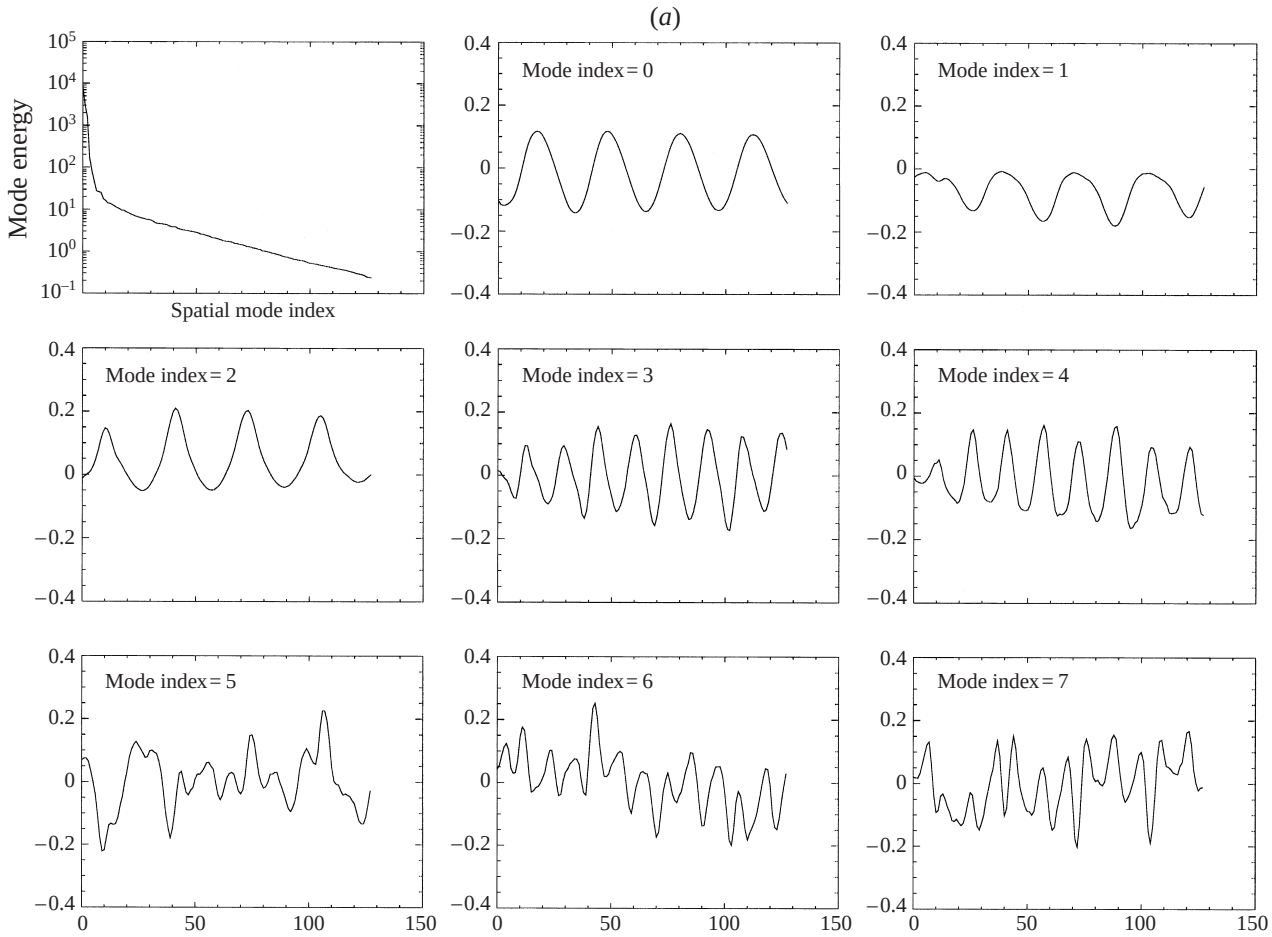

FIGURE 8 (*a*). For caption see opposite

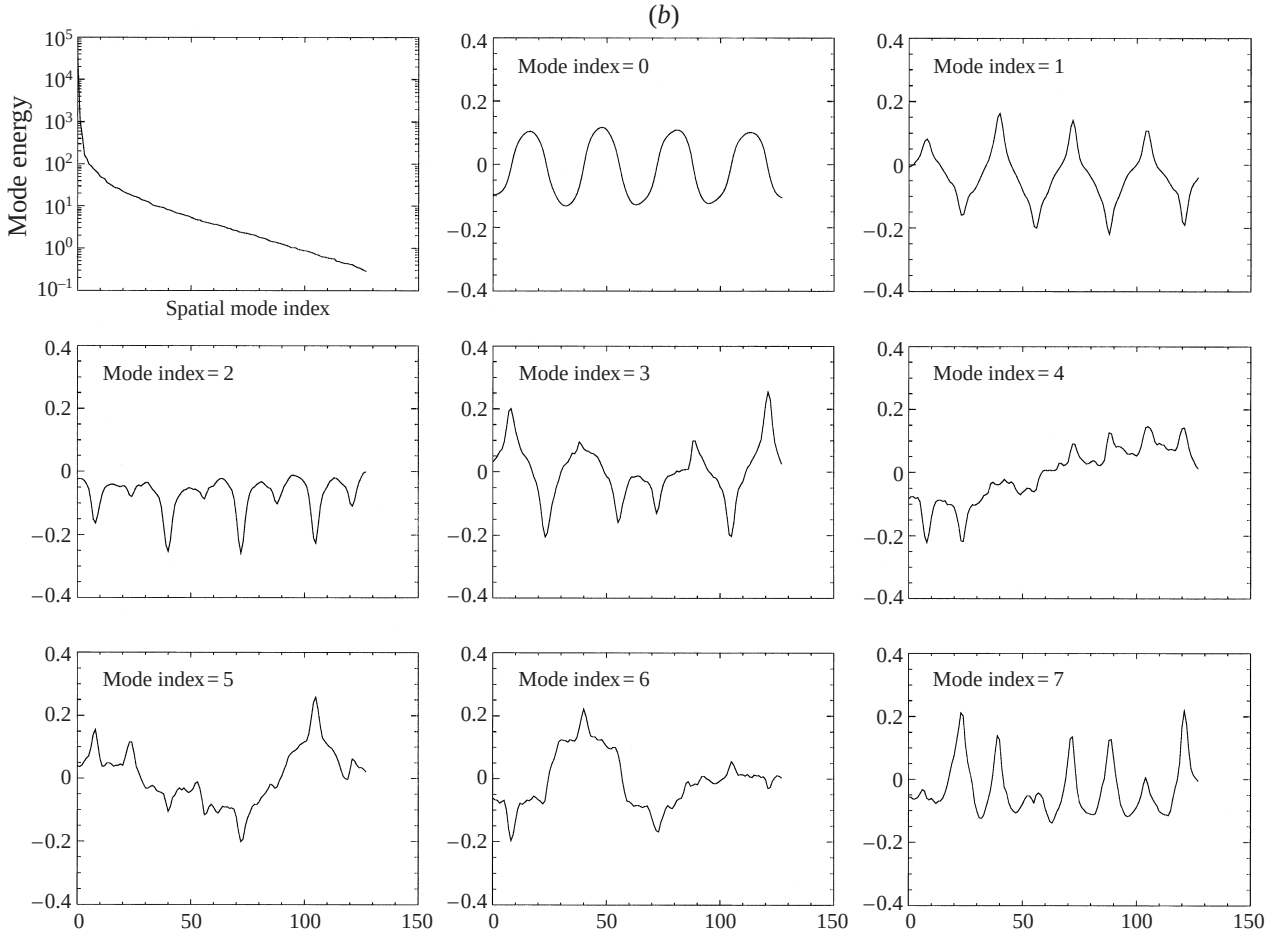

FIGURE 8. An example of the eigenvalue spectrum for $R^* = 13.63$ (top left) and eigenfunctions (up to 7) decomposed by orthogonal decomposition. The data are the same as for figure 3.

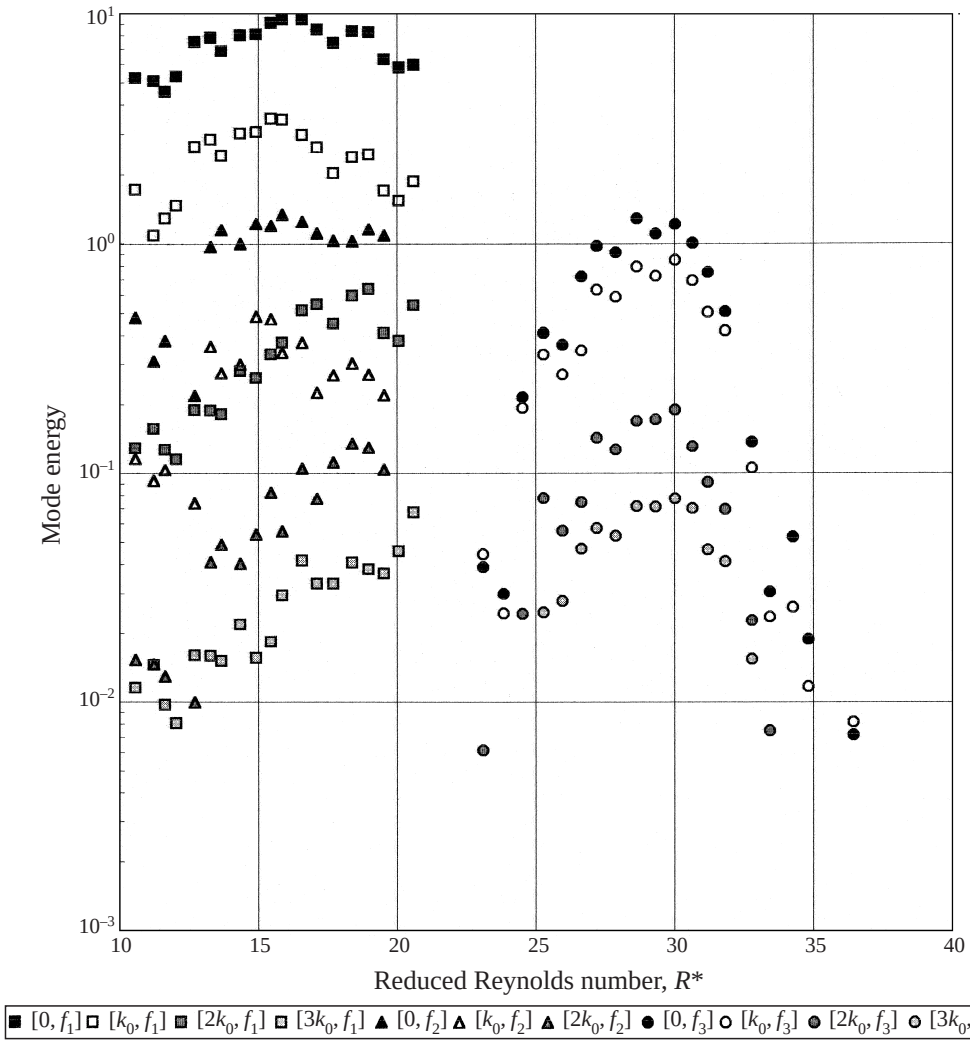

FIGURE 9. Variation of mode energy versus R^* for various modes identified in the two-dimensional-Fourier spectra. Solid points are identified as intrinsic modes while the others are their higher harmonics.

4.1.2. *Fast azimuthal wave*

To our knowledge, the third mode appearing at $R^* = 23$ has not been reported previously. The frequency of this mode is about 2.4 Hz ($3.5 f_{cyl}$), which is much higher than those of WVF and MWV modes. Moreover the amplitude is localized near the inflow and outflow boundaries and first identified using a two-dimensional Fourier spectrum.

Studying a spatio–temporal plot of the raw velocity field, as given in figure 2, and from the decomposed–reconstructed velocity field as shown in figure 10, this mode is attributed to the small but fast variation of velocity prevailing on the basic TVF rolls. Consequently we call this mode the 'fast azimuthal wave' mode. This mode has not been discussed nor quantitatively well studied to date. Walden & Donnelly (1979) reported that there appears a peak in the power spectrum for a similar range of R^*,

FIGURE 10. Decomposed and reconstructed velocity field of the mode newly found for $23 < R^* < 34$. Colour coding is the same as for figure 2.

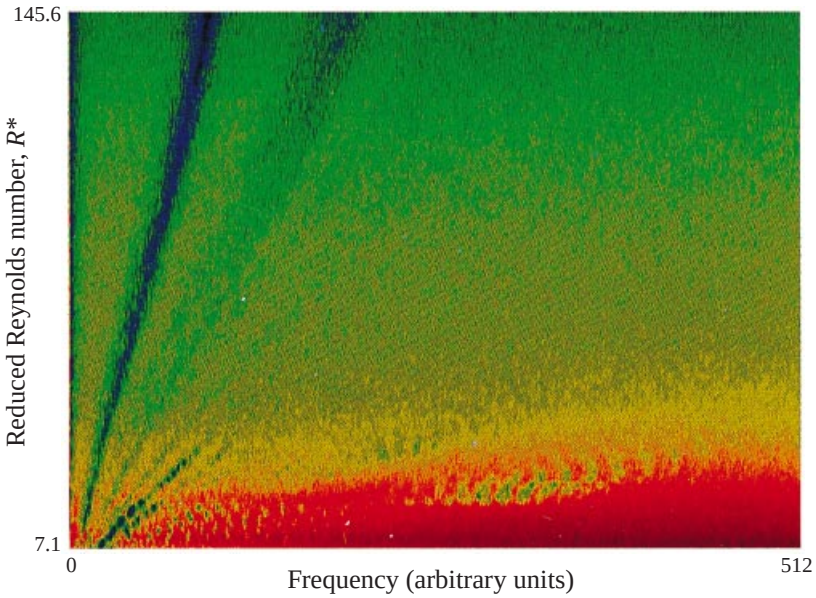

FIGURE 14. Variation of space-averaged power spectra on the (R^*, f)-plane. The power value is colour coded as in figure 2 but on a relative scale.

but only for a large aspect ratio system. They clearly stated that it would not appear for a system of the present configuration, namely for $\Gamma = 20$.

We also observed in the power spectra at very high frequency, for the same range of Reynolds number, a peculiar multiple peak (multiplet). Such a multiplet has also been observed by Swinney and collaborators using laser-Doppler velocimetry (H. L. Swinney, private communication; Reith 1981; Lewis 1996), but its nature has yet to be made clear. The fast azimuthal wave mode has a different frequency from this multiplet (and itself is not a multiplet); it requires further investigation. After the fast mode disappears at $R^* = 40$, the spectrum becomes continuous, showing no peak structure, except for the broad-band component f_B, which is discussed below.

4.2. *Orthogonal decomposition*

4.2.1. *Eigenvalues and eigenvectors*

Figure 11 shows the variation of the first 10 eigenvalues (mode index 0 is not included) with respect to Reynolds number. The overall behaviour is obviously quite similar to the one obtained by two-dimensional-FFT (figure 9). The first two modes have significant intensity and are approximately constant for $R^* < 21$ and then show a sharp decrease at $R^* \approx 21$. A broad peak is also seen at $R^* \approx 28$. We note that unlike Fourier modes, the eigenvectors of the orthogonal decomposition are data-dependent,

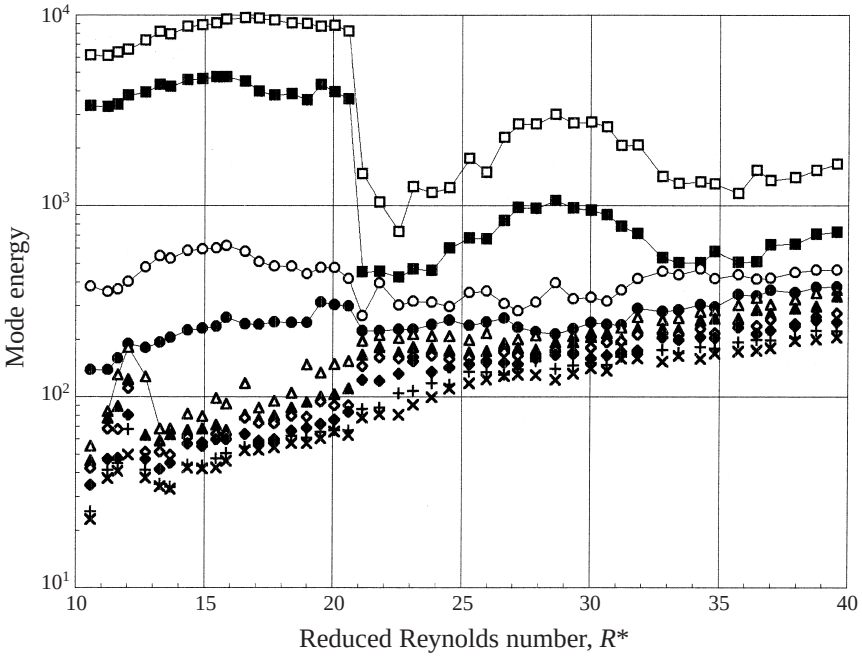

FIGURE 11. Variation of eigenvalues with R^* for the first 10 eigenmodes.

and hence it is not easy to trace the behaviour of a particular mode from the plot of eigenvalue vs. Reynolds number. This is especially true when a transition in flow behaviour occurs as a rather sharp change in flow character or the intensity of several modes is comparable. In such cases one has to investigate the changing shapes of the corresponding eigenvectors carefully. For example the top line (the strongest intensity) of figure 11 does not obviously refer to the same mode as that prevailing for the whole range studied here. From the results of Fourier analysis, it is understood that there are two distinct modes: one for $R^* < 21$ and the other for $R^* > 21$.

4.2.2. *Total energy occupation*

We consider two ways to quantify the complexity of the eigenvalue spectrum to make it easier to identify changes in flow behaviour as the Reynolds number is varied. They are (i) total energy occupation – discussed here, and (ii) global entropy – discussed below.

The total energy occupation (TEO) is defined as the number of modes which occupy 90% of the total signal energy, designated here as N_{90}. It is an index that reflects the magnitude of the number of participating modes in the flow field:

$$\sum_{i=0}^{N_{90}} \frac{e_i}{E_{total}} = 0.9, \tag{4.1}$$

where $E_{total} = \sum_{i=0}^{N} e_i$.

Figure 12 shows the variation of TEO with respect to Reynolds number. The value of N_{90} increases slowly from 2 to 7 over the range $9 < R^* < 21$. Then at $R^* = 21$ there is a jump to $N_{90} = 35$. Thereafter there is a regression to a local maximum at $R^* = 22$, followed by a slight decrease. For R^* less than 21, the eigenvectors of

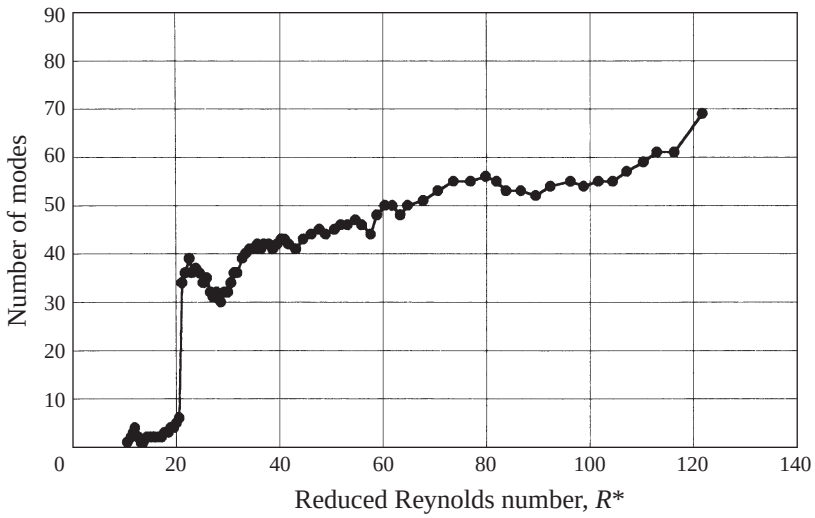

FIGURE 12. Variation of total energy occupation (TEO) versus R^*.

participating modes are more or less harmonic or at least highly periodic, while they are not for the larger R^*.

A local maximum is reached at $R^* \approx 22$ and a local minimum at $R^* \approx 28$. This reflects the broad peak behaviour of eigenvalues shown in figure 11. Since the dominant mode disappears at $R^* = 22$, the energy is shared by a larger number of modes. This causes the value of N_{90} to increase. For $23 < R^* < 32$ a new coherent mode appears, extracting a significant amount of energy from the flow, causing a decrease in the value of N_{90}. Beyond this point, N_{90} shows a gradual increase up to 55 at $R^* \approx 100$.

The large jump in N_{90} at $R^* = 21$ indicates the transition from CWV flow to TTV, and that the transition itself is quite sharp. However, the value of N_{90} itself remains finite – on the order of 40 to 60.

4.2.3. *Global entropy*

Aubry *et al.* (1994) suggested another way to use the information in the eigenvalue spectrum to identify changes in flow behaviour. They observed that the changing distribution of energy in the spectrum could be usefully characterized by a single number – the entropy of the spectrum (which they called global entropy). It is calculated as follows:

(i) compute normalized eigenvalues and interpret as probabilities: $p_i = e_i/E_{total}$;

(ii) compute global entropy as

$$H = -\frac{1}{\ln N} \sum_{i=0}^{N} p_i \ln p_i.$$

H ranges from 0 to 1. $H = 0$ corresponds to the perfectly ordered case (only one non-zero eigenvalue), and $H = 1$ corresponds to the completely disordered case (white spectrum – all eigenvalues equal). Figure 13 shows the variation of global entropy with respect to R^*: H is low, around 0.12, for R^* less than 19; at around $R^* = 21$, it shows a fairly sharp peak which then decreases to 0.13 at around $R^* = 29$, and then increases again to about 0.4. This behaviour corresponds to the transition scheme

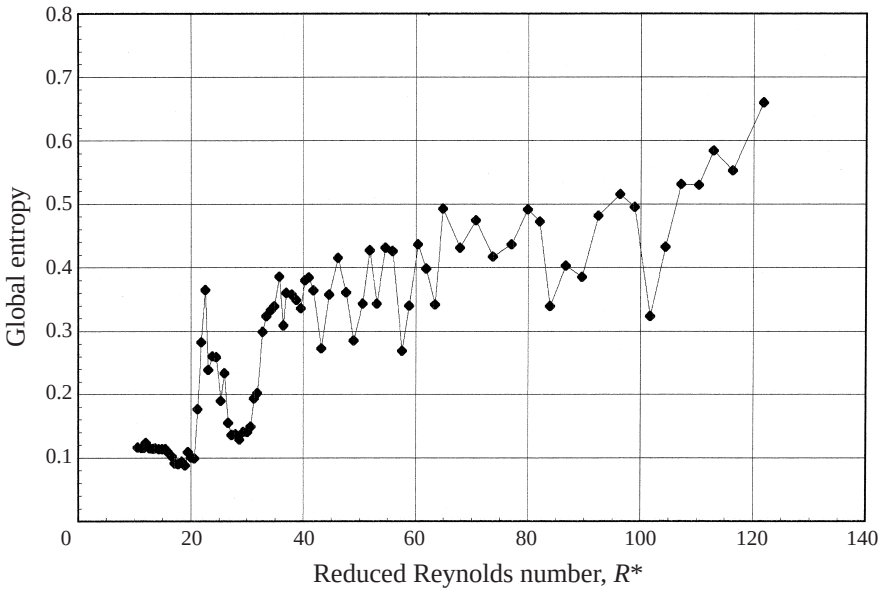

FIGURE 13. Variation of global entropy versus R^*.

discussed earlier. Since there are two coherent waves in CWV, global entropy remains small. When the intensity of these two modes decreases sharply, the entropy increases sharply. When the third wave mode appears above $R^* \approx 23$, the entropy again decreases, and then increases when this mode disappears. Such variation reflects the notion of global entropy, that is, it increases when the number of participating modes increases and as the energy becomes more uniformly distributed between these modes. In this context, the behaviour is quite similar to TEO as shown in figure 12. In the present case, a dip in the entropy at around $R^* \approx 23$ corresponds to the appearance of a new mode that occupies a considerable fraction of the total energy. We observe this concurrently as a dip of the curve in N_{90} versus R^*. It shows considerable fluctuation beyond $R^* > 40$, while the N_{90} curve in figure 12 is fairly smooth. The reason for this fluctuation is as yet unclear. It is, however, noted that our measuring method can resolve only up to 128 eigenmodes.

4.3. *Broad-band component*

For $R^* > 40$, there is no clear peak structure in the Fourier spectra. The eigenvectors from orthogonal decomposition also show no clear periodicity (except for the mean profile, i.e. the stationary TVF structure). This indicates that there is no longer any coherent azimuthal modal structure. Although we acknowledge that the time resolution of our measuring system is not sufficiently high for a highly turbulent flow, we nevertheless attempted to measure power spectra up to $R^* > 120$, as shown in figure 14 (p. 93). In this plot, no clear peak/line structure can be seen. However, a very broad peak remains which is attributed to the broad-band component, f_B. This may indicate a characteristic of the flow transition: a broad-band component is generated by some, as yet unknown, mechanism at relatively low Reynolds number. As R^* increases, all coherent structure disappears and only this broad-band component grows, seemingly leading to turbulence.

Rayleigh–Bénard	Taylor–Couette	Characteristics
Convection	TVF	Spatially periodic or symmetric
Oscillation	WVF	Temporally oscillating
Chaos	MWV/CWV	Quasi-periodic/chaos
Transition	Fast azimuthal wave mode	Still coherent-structural
Soft turbulence	Soft turbulence	Non-structural with soft spectrum
Hard turbulence	Hard turbulence	Non-structural with hard spectrum

TABLE 1. Similarity in transition states and corresponding flow regimes for convection and Taylor–Couette system.

4.4. *Soft turbulence*

In the range $40 < R^* < 80$, the values of N_{90} and the global entropy stay fairly constant. However, N_{90} takes on the finite values 40–60, while the global entropy is $H = 0.6$. From these results, we consider the flow for this range to be soft turbulence; that is, there is no coherent azimuthal structure which characterizes the flow field, and the energy is shared among a considerable number of modes, but the number of participating modes is still too small to be countable. The concept of 'soft' turbulence was introduced by Heslot *et al.* (1987) from convection experiments in helium gas. They investigated a scaling law of Nusselt number to Reynolds number and showed that the transition from laminar to turbulent progressed through various intermediate states as follows : convection–oscillation–chaos–transition–soft turbulence–hard turbulence. They used 'soft turbulence' to distinguish it from 'hard turbulence' based on the gradient of the scaling curve as well as the shape of the temperature probability density function (PDF). Our transition scheme is quite similar to this even though our flow configuration is quite different. The correspondence between the two cases is given in table 1.

Classification of turbulence has been attempted using PDFs of temperature fluctuations and by a scaling of flow characteristics with respect to Reynolds number (e.g. Castaing *et al.* 1989; Christie & Domaradzki 1993), or velocity structure functions (e.g. Benzi *et al.* 1995). They are mostly for a configuration of natural convection. We attempted such a classification for the Taylor–Couette system. In the sequence, we use the same terminology of 'soft turbulence'. The terms 'soft' and 'hard' are often used in the context of X-rays and neutron energy spectra. When these energy spectra extend to higher energy, the spectrum is called 'hard'. In contrast, when the fraction of the low-energy component is dominant, the spectrum is called 'soft'. In the present study, our observation is based on the power and energy spectra. Similar features have been seen in the space-averaged power spectrum, the time-averaged energy spectral density and eigenvalue spectrum. The spectra tend to increase their fraction of the large frequency or wavenumber portion at larger Reynolds number. This feature has been evaluated in quantitative manner using TEO and global entropy of the eigenvalue spectrum. For the ranges we classified as soft and hard turbulence, there exists a clear difference in the number of participating modes so that such a classification could be justified.

5. Conclusion

Spatio-temporal velocity fields, $V_z(z, t)$, have been measured and analysed quantitatively using Fourier transform and orthogonal decomposition techniques to investigate

transition from laminar flow to turbulence in a rotating Couette system. The Reynolds numbers studied here range from $R^* = 10$ to 40, and one study to $R^* = 120$. The results of FFT analysis show clear differences between various flow regimes. WVF and MWV have been clearly decomposed and their transition sequences have been made clear, especially that both modes disappear between $R^* = 21$ and 22.

A new mode was found to appear after the WVF and MWV modes disappear. From the decomposed velocity field, this mode is attributed to the fast variation of velocity on the TVF rolls and is called the fast azimuthal mode. The transition behaviour of this new mode was made clear by the form of the excitation curve of this mode. It appears at $R^* = 23$, reaches a maximum in its intensity at $R^* = 29$ and disappears at $R^* = 36$.

At still higher Reynolds number, there remains no coherent structure in the flow apart from the basic TVF and the broad-band components. Both Fourier spectra and eigenvalue spectra exhibit no characteristic peak structure and are continuous. This regime thus corresponds to TTV turbulence.

The characteristics of the continuous eigenvalue spectra were quantified using TEO and global entropy and the flow transition has been investigated quantitatively. Recall that TEO is the number of spatial modes containing 90% of the total energy. This means that we are counting the number of participating spatial degree of freedom. Global entropy indicates the degree of disorder of the flow state. The Reynolds number variations of these quantities show a clear difference in the dynamical behaviour of the different flow regimes. In particular, the transition to turbulence is fairly sharp, appearing as a sudden jump in the TEO and global entropy, but the number of participating modes is still too small to be countable. For this reason we classify the flow as 'soft' turbulence. This nature is found for the range of $R^* < 100$. Thus we propose the following classification in the Taylor–Couette system: laminar (Couette)–TVF–WVF–MWV–transition–soft turbulence–hard turbulence.

The author is grateful to M.-P. Chauve and P. Le Gal for a helpful discussion on orthogonal decomposition analysis and to G. King for his assistance in the computations, as well as fruitful discussions on the transition scheme.

REFERENCES

Aubry, N., Chauve, M. P. & Guyonnet, R. 1994 Transition to turbulence on rotating flat disk. *Phys. Fluids* **6**, 2804–2814.

Benzi, R., Ciliberto, S., Baudet, C. & Chavarria, C. 1995 On the scaling of 3-dimensional homogeneous and isotropic turbulence. *Physica* D **80**, 385–398.

Berkooz, G., Holmes, P. & Lumley, J. L. 1993 The proper orthogonal decomposition in the analysis of turbulent flows. *Ann. Rev. Fluid Mech.* **25**, 539–575.

Brandstater, A. & Swinney, H. L. 1987 Strange attractors in weakly turbulent Couette–Taylor flow. *Phys. Rev.* A **35**, 2207–2220.

Broomhead, D. S. & King, G. P. 1986 Extracting qualitative dynamics from experimental data. *Physica* D **20**, 217–236.

Burkhalter, J. E. & Koschmieder, E. L. 1973 Steady supercritical Taylor flows. *J. Fluid Mech.* **58**, 547–560.

Castaing, B., Gunaratne, G., Heslot, F. *et al.* 1989 Scaling of hard thermal turbulence in Rayleigh-Benard convection. *J. Fluid. Mech.* **204**, 1–30.

Christie, S. L. & Domaradzki, J. A. 1993 Numerical evidence for nonuniversality of the soft/hard turbulence classification for thermal convection. *Phys. Fluids* A **5**, 412–421.

Coles, D. 1965 Transition in circular Couette flow. *J. Fluid Mech.* **21**, 385–425.

Coughlin, K. T., Marcus, P. S., Tagg, R. P. & Swinney, H. L. 1991 Distinct quasiperiodic modes with like symmetry in a rotating fluid. *Phys. Rev. Lett.* **66**, 1161–1164.

Di Prima, C. & Swinney, H. L. 1985 Instabilities and Transition in Flow Between Concentric Rotating Cylinders. In *Hydrodynamic Instabilities and the Transition to Turbulence* (ed. H. L. Swinney & J. P. Gollub), p. 139. Springer.

Drazin, P. G. & King, G. P. 1992 Introduction to the proceedings of the workshop 'The Interpretation of Time Series from Nonlinear Mechanical System'. *Physica* D **58**, vii–xi.

Fenstermacher, P. R., Swinney, H. L. & Gollub, J. P. 1979 Dynamical instabilities and the transition to chaotic Taylor vortex Flow. *J. Fluid Mech.* **94**, 103–128.

Gorman, M. & Swinney, H. L. 1979 Visual observation of the second characteristic mode in a quasiperiodic flow. *Phys. Rev. Lett.* **43**, 1871–1874.

Heslot, F., Castaing, B. & Libchaber, A. 1987 Transition to turbulence in helium gas. *Phys. Rev.* A **36**, 5870–5873.

King, G. P. & Swinney H. L. 1983 Limits of stability and irregular flow patterns in wavy vortex flow. *Phys. Rev.* A **27**, 1240–1243.

Koschmieder, E. L. 1979 Turbulent Taylor vortex flow. *J. Fluid Mech.* **93**, 515–527.

Koschmieder, E. L. 1980 Transition from laminar to turbulent Taylor vortex flow. In *Laminar-Turbulent Transition* (ed. R. Eppler & H. Fasel) *IUTAM Symposium, September 16–12, 1979 Stuttgart, Germany*. Springer.

Lathrop, D. P., Fineberg, J. & Swinney, H. L. 1992 Transition to shear-driven turbulence in Couette–Taylor flow. *Phys. Rev.* A **46**, 6390–6405.

Lewis, G. 1996 Velocity fluctuations, wall shear stress and the transition in torque scaling at $R = 13,000$ in turbulent Couette-Taylor flow. PhD thesis, University of Texas, Austin.

Lumley, J. L. 1967 The structure of inhomogeneous turbulent flow. In *Atmospheric Turbulence and Radio Wave Propagation* (ed. A. M. Yaglom & V. I. Tatarski), pp. 166–178. Moscow: Nauka.

Lumley, J. L. 1981 Coherent structures in turbulence. In *Transition and Turbulence* (ed. R. E. Meyer), pp. 215–242. Academic.

Reith, L. A. 1981 Transition to turbulence in a circular Couette system. PhD thesis, University of Texas, Austin.

Sirovich, L. 1991 Empirical Eigenfunctions and Low Dimensional systems. In *New Perspectives in Turbulence* (ed. L. Sirovich). Springer.

Takeda, Y. 1986 Velocity profile measurement by ultrasound Doppler shift method. *Intl J. Heat Fluid Flow* **7**, 313–318.

Takeda, Y. 1990 Development of ultrasound velocity profile monitor. *Nuclear Engng Design* **126**, 277–284.

Takeda, Y. Fischer, W. E. & Sakakibara, J. 1993*a* Measurement of energy spectral density of a flow in a rotating Couette system. *Phys. Rev. Lett.* **70**, 3569–3571.

Takeda, Y. Fischer, W. E. & Sakakibara, J. 1994 Decomposition of the modulated waves in a rotating Couette system. *Science* **263**, 502–505.

Takeda, Y., Fischer, W. E., Sakakibara, J. & Ohmura, K. 1993*b* Experimental observation of the quasiperiodic modes in a rotating Couette system. *Phys. Rev.* E **47**, 4130–4134.

Teufel, M., Trimis, D., Lohmuller, A., Takeda, Y. & Durst, D. 1992 Determination of velocity profile in oscillating pipe-flow by using laser Doppler velocimetry and ultrasonic measuring devices. *Flow Meas. Instrum.* **3**, 95–101.

Walden, R. W. & Donnelly R. J. 1979 Reemergent order of chaotic circular Couette flow. *Phys. Rev. Lett.* **42**, 301–304.

Zhang, L. H. & Swinney, H. L. 1985 Nonpropagating oscillatory modes in Couette–Taylor flow. *Phys. Rev.* A **31**, 1006–1009.